Immersed Boundary Wall-Modelled Large Eddy Simulations of Subsonic Jet Flows and Acoustics

Man Long Wong *, Aditya S. Ghate, Gaetan K. W. Kenway, Jordan B. Angel, and Cetin C. Kiris
Volcano Platforms Incorporated, Palo Alto, CA 94304, USA

Jet simulations with an axisymmetric nozzle are used to validate an octree Cartesian Navier–Stokes solver, *Volcano ScaLES*, with Wall-Modelled Large Eddy Simulation (WMLES) capability. Several subsonic jet flows with varying acoustic Mach numbers and temperature ratios exhausted from the NASA's SMC000 nozzle are simulated to assess the capability of the GPU-accelerated scale-resolving solver in predicting the turbulent jet flows and far-field aeroacoustics. The mean velocity and Reynolds stress profiles are sampled directly using the simulation data and compared with the near-field experimental results. The acoustics at far-field microphone locations are approximated using the near-field flow data collected on multiple permeable surfaces with the Ffowcs Williams–Hawkings acoustic analogy. The accuracy in predicting the far-field noise spectra at different microphone angles with the variations of acoustic Mach number and temperature ratio are also assessed using the experimental results.

I. Introduction

Aircraft noise has detrimental effects on the health of humans living near airports. The aircraft noise is mainly generated from sources of the airframe and propulsion system. While there have been continuous progress in the reduction of propulsion noise of civil aircrafts by at least 20 dB since 1960s, such as through the use of large bypass ratios of turbofan engines, acoustic liners, chevron nozzles, active noise control, etc. [1], propulsive jet noise still dominates the overall civil aircraft noise during takeoff and flyover conditions. The NASA Advanced Air Transport Technology (AATT) has set a noise reduction goal of over 40 Effective Perceived Noise Level in decibels (EPNL dB) cumulative below the Stage 4 FAA noise requirement for the far term period of 2035 [2]. Meanwhile, the Advisory Council for Aviation Research and Innovation in Europe (ACARE) and the Flightpath 2050 project [3] targeted a 65% reduction of the perceived noise by 2050, with respect to the noise levels in 2000. To meet with these increasingly stringent noise reduction goals, the design of more quiet engines is critical to decrease the overall aircraft noise. The jet propulsion noise is primarily caused by the turbulent mixing between the exhaust gas and the atmospheric air. Therefore, it has a strong dependence on the jet velocity or the jet Mach number M_j ($\sim M_j^8$ [4]). Through the use of large engine bypass ratio, the jet exhaust velocity can be largely reduced for lower jet noise while the same level of thrust is maintained. Nevertheless, this also leads to more severe secondary effects such as airframe noise generation due to the closer interaction between the jet plume and the high-lift devices. The investigation of the mechanism of secondary effect on noise generation from the jet interaction with airframe is still an ongoing research [5, 6]. To improve the design of more quiet engines with more complicated noise generating mechanisms, there is an increasing demand on the use of Computational Fluid Dynamics (CFD) and Computational Aero-Acoustics (CAA) tools for accurate predictions of jet aeroacoustics over the years.

Due to the large range of turbulent scales generated during the violent mixing between the jet plume and the ambient gas, the jet noise is broadband. The Large Eddy Simulation (LES) provides a computationally feasible way to resolve this wide range of spatio-temporal turbulent scales for acoustic predictions. A successful prediction of the turbulent compressible mixing and the propagation of acoustic waves over a large distance ($O(10)\times$ wavelength) from the acoustic sources requires attention in many details, such as the numerical discretization, the grid resolution, the inclusion of the boundary layer effects from the nozzle geometry, as pointed out in the review written by Bodony and Lele [7]. In the last decade, there has been a large progress in the application of LES for practical jet noise predictions with physical nozzle geometry at higher Reynolds number (over 1 million) due to the improvement in numerical methods, meshing, wall modelling, and advancements in high-performance computation [8]. The advancement in meshing is generally coupled with the application of minimum dissipation and high resolution numerical methods for jet simulations with complex nozzle geometries. In general, the meshing methodologies used for jet LES computations can be classified into the body-fitted methods or Cartesian immersed boundary methods. The use of curvilinear meshes with a low dissipative

*Corresponding author.

Weighted Compact Nonlinear Scheme [9, 10], and the Voronoi unstructured grids with low-dissipation kinetic energy and entropy preserving numerical methods [11] are examples of body-fitted meshing topology for jet aeroacoustics computations, whereas the use of Cartesian mesh with immersed boundary method has been demonstrated with the Lattice Boltzmann Method (LBM) [6, 12, 13]. In recent years, there have been an increased popularity in the use of Wall-Modelled Large Eddy Simulation (WMLES) for studying jet acoustics with nozzle geometries under different flow configurations [10, 14–18]. In this approach, the wall-stress boundary conditions provided by the wall models eliminate the need to resolve the thin turbulent boundary layer and largely reduce the grid cells and computational expenses.

In this work, a state-of-the-art compressible Navier–Stokes Cartesian solver based on octree Cartesian grids, the Volcano ScaLES, is used for the simulations of subsonic turbulent jet flows with the associated far-field aeroacoustics using Graphics Processing Units (GPUs). The use of compressible Navier–Stokes formulation enables the simulations of subsonic, transonic, and supersonic isothermal and thermal jet flows with the same solver. This is unlike the traditional LBM which is not suitable for high Mach and non-isothermal flows unless large modifications on the LBM are made the capture the high Mach and thermal effects in the simulations. The Volcano ScaLES also has the immersed boundary method implemented with the WMLES capability. The capability of the solver in predicting the near-field flow statistics is examined in details in this work with grid sensitivity study. Furthermore, the near-field solutions are radiated to the far-field microphone locations using the permeable Ffowcs Williams–Hawkings method as the acoustic analogy. The sensitivities of the sampling surface location, as well as the grid resolution, on the far-field noise approximation are studied and compared with the experimental results.

II. Description of Problem

The subsonic jets of air emitted from an axisymmetic nozzle, the NASA's baseline Small Metal Chevron (SMC000) nozzle, are considered in this work. The nozzle has a round inlet with 152 mm (6 in) diameter, followed by a sharp contraction section with a final taper of 5° at the exit [19]. The nozzle exit at $x = 0$ has a diameter of $D = 0.0508$ m (2 in) with a lip thickness of 1.524 mm (0.06 in). There is a well established database of experimental measurements of subsonic jet flows under different operation conditions for this nozzle geometry [20, 21]. In this work, five setpoints (SP), SP03, SP07, SP23, SP27, and SP46, are simulated. Among these five setpoints, SP03 and SP23 have similar acoustic Mach numbers, $M_a = U_j/c_\infty$, at around 0.5, where U_j is the expected jet velocity magnitude at the nozzle exit and c_∞ is the ambient sound speed, while SP07, SP27, and SP46 have similar M_a at around 0.9. SP03 and SP07 have essentially isothermal jets, where the jet temperature values are similar to the corresponding ambient temperature values. On the other hand, SP23, SP27, and SP46 have heated jets where the temperature ratios between the jet exhaust temperature, T_j, and the ambient air temperature, T_∞, TR = T_j/T_∞, are both near 1.8 for the first two setpoints and is around 2.7 for SP46. The Reynolds number based on U_j, D and the exit jet density, ρ_j, varies between 0.40 and 1.46 million, where the viscosity is computed with the Sutherland's law using T_j. The operating conditions of all setpoints are tabulated in Table 1.

Setpoint	M_a	M_j	T_∞ [K]	TR (T_j/T_∞)	NPR (p_t/p_∞)	NTR (T_t/T_∞)	Re_D	U_j/D [Hz]
SP03	0.500	0.512	286.50	0.955	1.1956	1.0050	0.6361×10^6	3339.7
SP07	0.902	0.983	283.18	0.842	1.8560	1.0047	1.4617×10^6	5989.9
SP23	0.492	0.370	278.20	1.764	1.0994	1.8124	0.2217×10^6	3238.4
SP27	0.901	0.678	280.10	1.764	1.3609	1.9264	0.4028×10^6	5950.6
SP46	0.901	0.548	281.00	2.702	1.2266	2.8644	0.1983×10^6	5960.2

Table 1 Operating conditions of the setpoints [20, 21] chosen for this study. $M_a = U_j/c_\infty$ is the acoustic Mach number based on the expected jet velocity magnitude at the nozzle exit, U_j, and ambient sound speed, c_∞. $M_j = U_j/c_j$ is the jet Mach number based on the jet sound speed, c_j, at the nozzle exit. Temperature ratio, TR, is the ratio between the jet temperature, T_j, and the ambient temperature, T_∞. NPR and NTR are the nozzle pressure and temperature ratios, where T_t and p_t are the stagnation temperature and pressure at the plenum and p_∞ is the ambient pressure. Re_D is the Reynolds number based on the nozzle exit diameter, D, and the expected velocity magnitude, U_j, density, ρ_j, and temperature, T_j, of the jet at the nozzle exit. Note that U_j/D is the characteristic frequency.

III. Details of Simulations

A. Numerical Methods

The GPU-accelerated scale-resolving solver, Volcano ScaLES, is used for all the LES computations in this work. The compressible Navier–Stokes equations are solved where the inviscid flux is discretized with a fourth order finite difference scheme with favorable kinetic energy and entropy consistency properties, making it suitable for LES over a vast range of flow regimes. The viscous flux discretization utilizes a mix of fourth and second order discretizations with improved resolution which has good accuracy and robustness for high Reynolds number turbulent flows, without the need of numerical dissipation through the inviscid flux numerical operator in turbulence resolving regions. The overall numerical scheme has minimum numerical dissipation, even when the shock-capturing capability is enabled, using physics-based sensors that are functions of local velocity gradients as well as strong thermodynamics fluctuations. Additional methods to reduce generation of spurious numerical noise at walls as well as at coarse-fine grid interfaces are also utilized in the present work. Key convenience provided by the Cartesian grids with unit aspect ratio is that the use of explicit time-stepping scheme becomes feasible even in flows involving highly complex geometries as the perfectly isotropic grid cells near the geometry do not introduce any numerical stiffness associated with complex grid topologies. The time integration is performed using the explicit third order strong-stability-preserving Runge–Kutta time stepping scheme [22]. Note that the shock-capturing capability is completely turned off in all of the simulations presented in this work.

Geometries are represented in the computations using a sharp immersed boundary method capable of enforcing inviscid no-penetration boundary conditions as well as viscous skin friction with appropriate Reynolds number asymptotic properties using an equilibrium wall model. In this WMLES approach, only the outer boundary layer eddies are resolved while the subgrid eddies in the inner boundary layer are modeled with the wall model. This largely eliminates the need to resolve the turbulent boundary layer using very fine grid cells and reduces the computational expenses. The wall model that provides a wall shear stress constraint uses solution information interpolated via probing at a fixed distance of 1.5Δ into the fluid away from walls, where Δ is the local grid spacing at the wall. All simulations presented in this work utilize the constant coefficient Vreman subgrid scale (SGS) closure [23] with constant turbulent Prandtl number to model the subgrid scales.

The CFD solver has been validated using a sequence of WMLES including: a) airframe noise [24], b) vibro-acoustics of a launch vehicle [25], c) aerodynamics of iced straight wings [26], d) F-16XL aircraft aerodynamics [27], and e) automotive aerodynamics [28].

B. Computational Architecture

Motivated by the need to fully exploit all available resources on modern GPUs, Volcano ScaLES is written exclusively in C++ and CUDA. On simulations involving non-canonical geometries such as those considered in this paper, we achieve approximately 30% of peak FLOPs on compute-oriented devices along with nearly perfect (> 95%) weak scaling efficiency from 1 to 8 GPUs. Unlike most CFD codes, the majority of the computations are compute bound and we achieve high performance even in graphics-oriented, bandwidth-restricted devices, such as the Nvidia GeForce RTX 4090. The combination of Cartesian methods and an explicit time stepping scheme yields extremely low memory requirements: ScaLES can simulate between 8.5 and 10 million cells per gigabyte of GPU memory depending on the complexity of the configuration. Simulations containing between 400 and 500 million cells are routinely performed on desktop computers containing just two RTX 4090 GPUs with 24 Gb of memory each.

C. Problem Setup

All simulations are conducted with a coflow Mach number of 0.005 to help flush out the eddies generated at the shear layers during the transient stage of the simulations to accelerate the convergence of statistics. The inlet is placed at around $8D$ upstream of the nozzle exit plane with the inflow boundary conditions prescribed using the stagnation pressure and temperature. Equilibrium wall model is used at all solid boundaries of the nozzle to provide the shear stress boundary conditions for the momentum equations. In addition, adiabatic boundary condition is used for the total energy equation at the geometry.

Two different Cartesian octree grids, A and B, with similar grid topologies but different finest grid spacings are generated for the numerical study in this work using the Volcano meshing software. These two grids are depicted in Figure 1. The Volcano meshing software creates Cartesian grids using a recursive octree approach. Grids around practical configurations consist of a unstructured grids of millions of “boxes” each of which contains a structured grid of 4^3 or 8^3 cells. This method gives nearly all the computational advantages of structured grids while retaining the

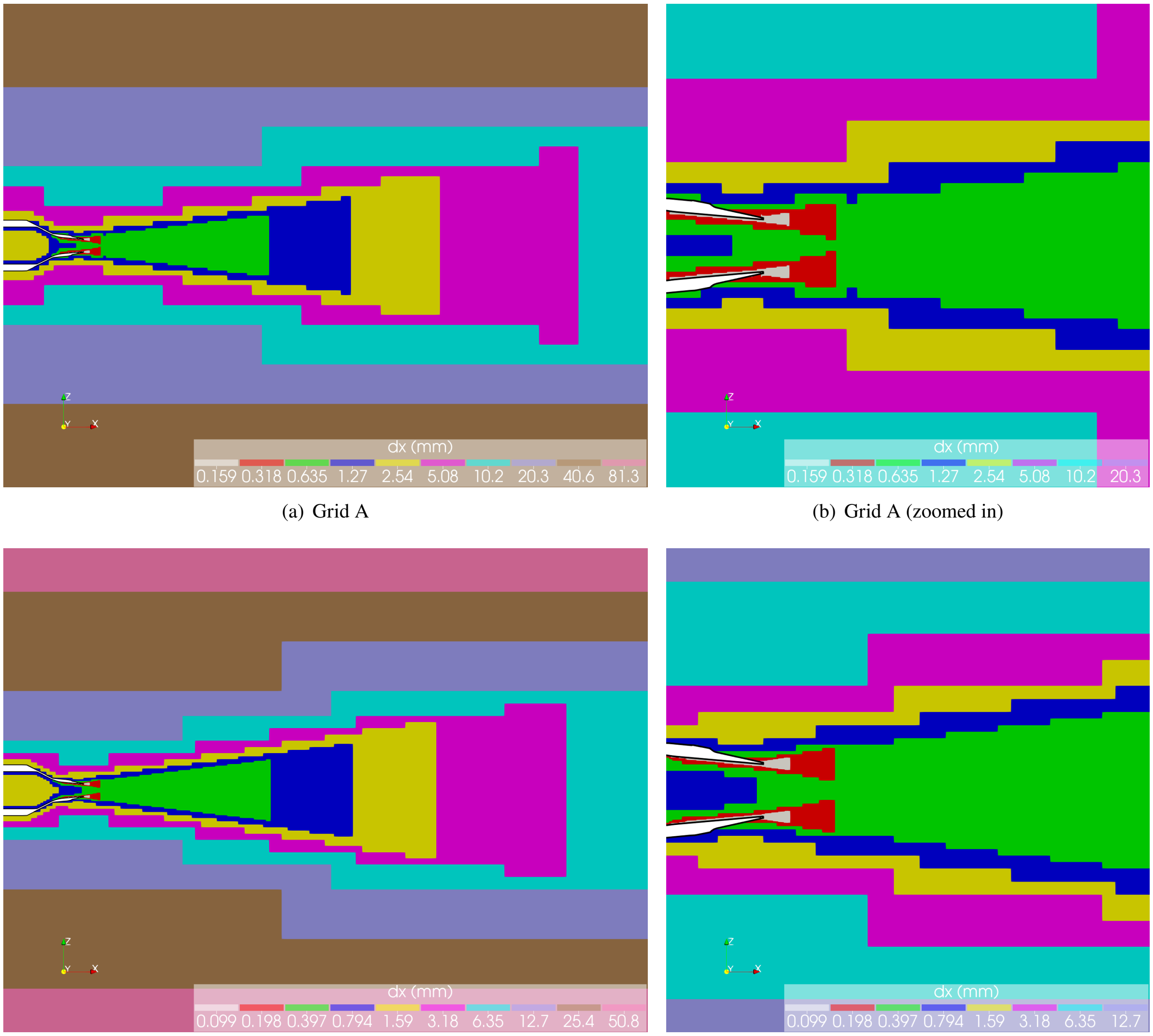

(a) Grid A

(b) Grid A (zoomed in)

(c) Grid B

(d) Grid B (zoomed in)

Fig. 1 Cross-sections of different grids at the center-plane ($y = 0$) showing the grid topologies with the grid spacings. The black contour lines show the location of the nozzle.

ability to closely follow surfaces and minimize the number of "dead" cells inside the geometry. Typically, 90-95% of the total cells in a grid are compute cells, while the remaining ones are considered "dead" or "blanked" cells. Grids A and B have finest grid spacings of 0.15875 mm and 0.09921875 mm respectively. For both grids, the regions near the inner nozzle surface close to the nozzle exit including the lip are refined to the finest mesh level. These corresponds to 9.6 and 15.36 cells across the lip thickness for grids A and B respectively. Inside the nozzle from $x = -1.5D$ to the nozzle exit, constant thickness heights of roughly 10 and 16 grid cells are used for the finest level near the inner nozzle surface such that a roughly constant thickness height of 1.59 mm is maintained when grid A is refined to grid B. Two hollow tapered cylindrical refinement regions at the finest and second finest mesh levels are applied near the lip of the nozzle until $x = 0.5D$ and $x = 1.35D$ respectively to improve the accuracy in simulating the turbulent transition at the shear layers. Another tapered cylindrical refinement region at the third finest mesh level is used for resolving the turbulent eddies of the jet plume near the nozzle from $x = 0$ to $x = 15D$ for each grid. This grid resolution for the jet plume corresponds to 80 and 128 points per D. Beyond this cylindrical refinement region, five more tapered cylinders with increasing end base diameter and location from the lip but decreasing grid resolution are used to assist the gradual grid coarsening. Worth mentioning, the tapered cylindrical region at the fifth finest mesh level is designed to start from $x = 21.5D$ to $28D$ to contain all endcaps of the sampling surfaces for far-field aeroacoustic wave propagation, which will be discussed in a later section. The grid hierarchies of grids A and B are shown in Figure 1, which have 143.70 and 524.93 million compute cells, respectively. All simulations with grids A and B are respectively conducted until 1600th and 1000th convective time unit (CTU) defined with D and U_j, i.e., CTU = D/U_j. Statistics are collected from the 400th CTU after the initial transient is flushed out for each simulation. The details of all simulations including the grid statistics and the computational resources used are shown in Table 2.

Setpoint	Grid label	Minimum grid spacing (mm)	Number of compute grid cells (million)	Averaged time step size (μs)	Number of CTUs	Number of GPUs used	Wall-clock hours per 100 CTUs
SP03	A	0.159	143.70	0.2152	1600	2 x GeForce RTX 4090	2.175
	B	0.099	524.93	0.1331	1000	2 x GeForce RTX 4090	9.679
SP07	A	0.159	143.70	0.1888	1600	2 x GeForce RTX 4090	3.035
	B	0.099	524.93	0.1164	1000	2 x GeForce RTX 4090	6.205
SP23	A	0.159	143.70	0.1748	1600	2 x GeForce RTX 4090	2.854
	B	0.099	524.93	0.1095	1000	2 x GeForce RTX 4090	13.204
SP27	A	0.159	143.70	0.1550	1600	2 x GeForce RTX 4090	2.275
SP46	A	0.159	143.70	0.1295	1600	2 x GeForce RTX 4090	2.329

Table 2 Details of different jet simulation cases.

In all of these simulation cases, tripping of the boundary layer inside the nozzle is performed to facilitate the turbulent transition of the boundary layer near the nozzle exit. Similar tripping dots [10] or annular zigzag trips [13] were used in previous studies to trigger fluctuations at the boundary layers for these setpoints. In this work, the tripping location is defined using a fence on any walls, where the location of the immersed boundary is perturbed using a tripping height. In this work, a circular tripping fence is placed on the inner nozzle surface at $x = -1.5D$ upstream of the nozzle exit plane. The tripping heights used are 0.238 mm and 0.149 mm for grids A and B respectively, which correspond to around 1.5Δ for each grid. From the surface skin friction on the inner wall and the velocity fields close to the nozzle exit, we have verified that the boundary layers are fully turbulent in all simulations. As an example, the surface skin friction coefficient magnitude on the inner nozzle wall and the Mach number contours in Figure 2 show that the boundary layers near the exit are fully turbulent for both SP03 simulations with grids A and B. It should also be noted that the entire turbulent boundary layers near the nozzle exit are designed to be covered by the finest level grid cells.

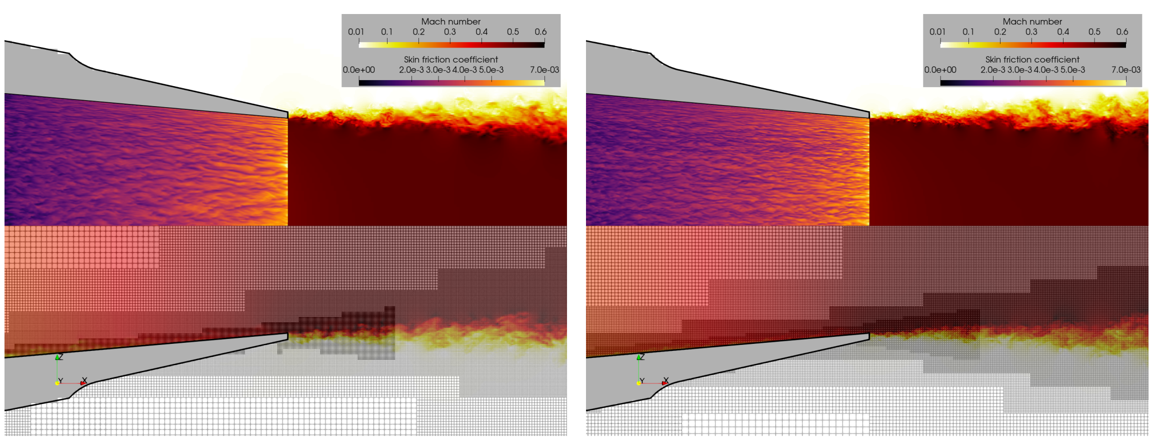

(a) Grid A

(b) Grid B

Fig. 2 Skin friction coefficient magnitude on the upper half of the inner nozzle surface from the SP03 simulations using different grids. The center-plane slice shows Mach number contours inside and outside the nozzle. Tripping upstream at the inner nozzle wall ensures fully turbulent boundary layer state when the jet exits the nozzle.

IV. Computational Results and Discussions

This section discusses both the near-field and far-field computational results of all simulation cases. In all of these computations, the near-field statistics are collected directly from the WMLES after 400 CTUs for each case until the end of the simulations. As for the far-field acoustics, the pressure fluctuations are computed with near-field data sampled on surfaces enclosing the turbulent jet plume using an acoustic analogy after 400 CTUs. This section is split into the two parts. In the first part, near-field flow dynamics are visualized and compared between different setpoints. The capabilities of the WMLES in predicting the near-field flow statistics under the compressibility and thermal effects are also examined through comparison of the WMLES results with the experimental data. In the second part, the set up of the near-field sampling surfaces for far-field radiation will be described. The accuracy in the use of the LES results with the permeable Ffowc Williams–Hawkings acoustic analogy for prediciting far-field noise will be analyzed for all setpoints.

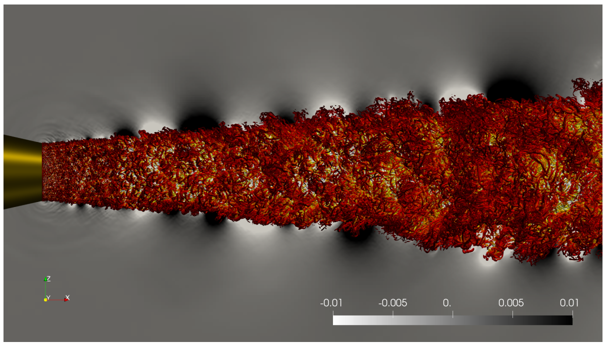

(a) SP03, grid B

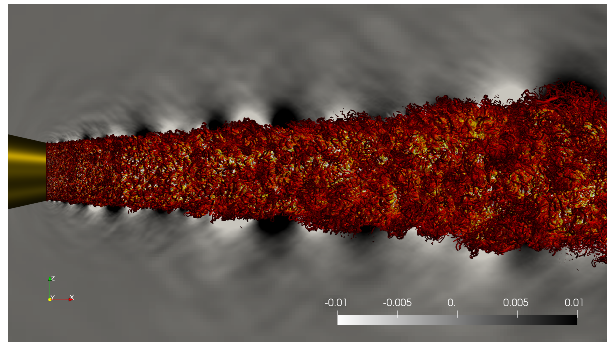

(b) SP07, grid B

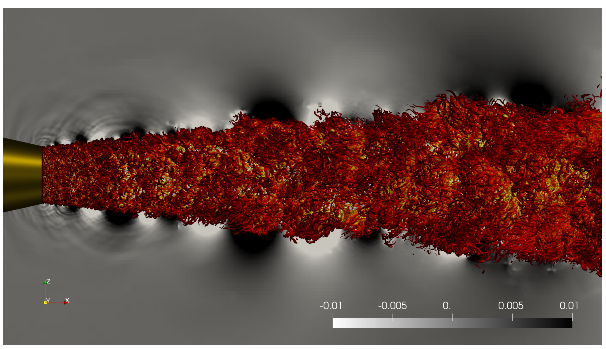

(c) SP23, grid B

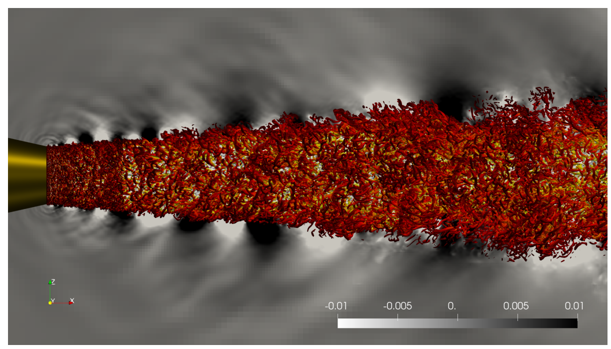

(d) SP27, grid A

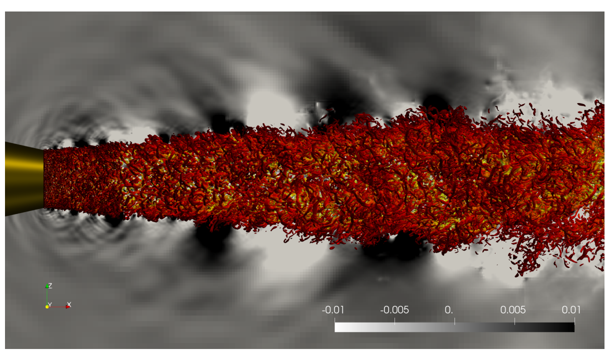

(e) SP46, grid A

Fig. 3 Iso-surfaces of the Q-criterion normalized by the convective time unit, CTU, at the value of 3.5, on top of the center-plane slice showing the instantaneous pressure coefficient, C_p, based on the jet exit density, velocity magnitude, and the ambient pressure for different setpoints. The iso-surfaces of Q-criterion are colored by Mach number which ranges from zero to 0.2 for SP03 and SP23, zero to 0.4 for SP07, SP27, and SP46.

A. Near-field Flow Dynamics

1. Near-field Flow Visualizations

Figure 3 shows the iso-surfaces of the Q-criterion, normalized by the CTU, computed with the highest grid resolution simulation for each setpoint. From the iso-surfaces, rapid breakdown of the eddies at the shear layers around the lip of the nozzle can be clearly seen for all setpoints. As the turbulent vortices advect downstream, the shear layers spread in the radial direction. In general, the jets of the setpoints at lower $M_a \approx 0.5$ spread radially at faster rates compared to those at $M_a \approx 0.9$. The center-plane slice displays the instantaneous pressure coefficient, $C_p = 2(p - p_\infty)/(\rho_j U_j^2)$, for each case where p is the pressure. Comparing the two isothermal jets, SP03 and SP07, stronger acoustic waves are scattered for the latter case which has higher acoustic and jet Mach numbers. Similar observations are found by

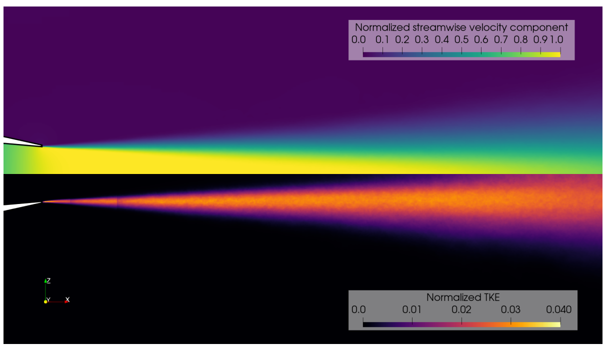

(a) SP03, grid B

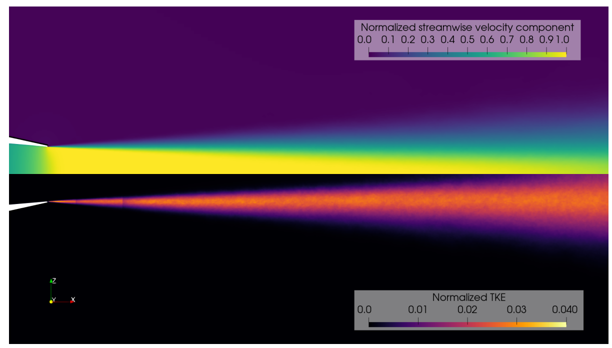

(b) SP07, grid B

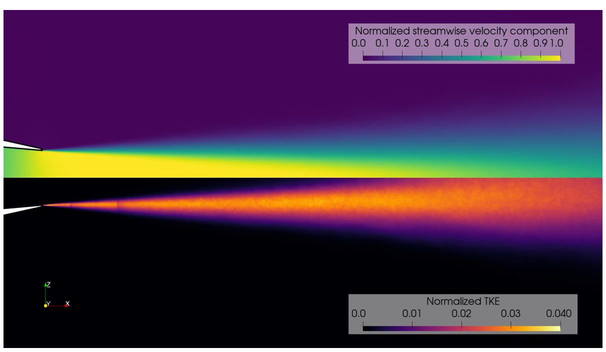

(c) SP23, grid B

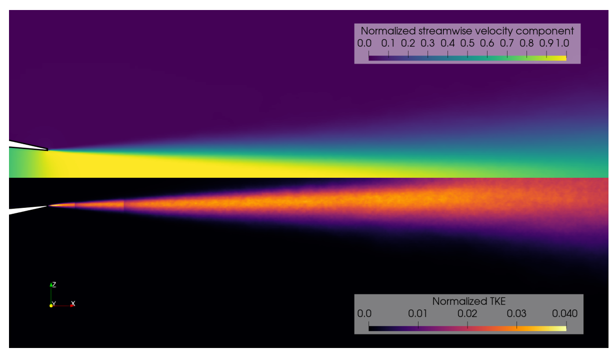

(d) SP27, grid A

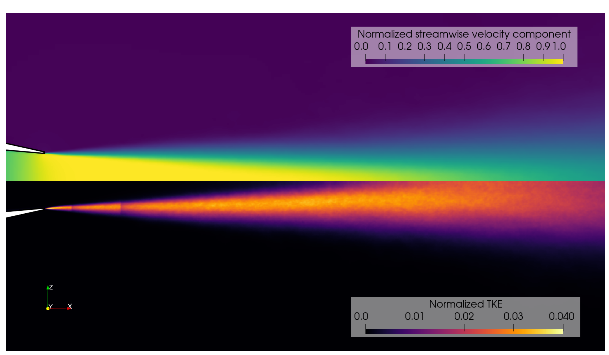

(e) SP46, grid A

Fig. 4 Mean (time-averaged) streamwise velocity component and turbulent kinetic energy (TKE) normalized by the jet exit density U_j for different setpoints. The top half of each figure shows the normalized mean streamwise velocity component; while the bottom half shows the normalized TKE.

comparing the two cases with TR ≈ 1.8, SP23 and SP27, where the latter produces stronger acoustic waves due to higher Mach number. On the other hand, with similar M_a, the intensity of the acoustic waves, specifically near the lip, increases with the TR, as can be seen easily by comparing the C_p fields of cases SP07, SP27, and SP46 (or similarly for SP03 and SP23).

Figure 4 displays the mean streamwise velocity components, $\overline{u}$, and the turbulent kinetic energy (TKE), TKE = $\overline{u'u' + v'v' + w'w'}/2$, for each setpoint, where $u = \overline{u} + u'$ for the streamwise velocity u and $\overline{(\cdot)}$ is the time-averaging (same Reynolds decomposition for velocity components in the y- and z-directions, v and w). Both $\overline{u}$ and TKE are normalized using U_j. For all setpoints, the velocity magnitude outside the nozzle exit quickly reaches the corresponding U_j in the simulations. From the plots, it can be seen that the mixing between the jet and the ambient air causes the shear layers to grow and spread in the radial direction, originated from the lips. Eventually, the shear layers collapse in the radial direction from opposite sides and the potential cores with almost uniform velocity magnitude at U_j disappear. In addition, while the flow becomes very turbulent immediately at the lip with very high TKE for each case, the TKE keeps increasing along the lipline for a distance before decaying. Comparing SP03 and SP23 which both have $M_a \approx 0.5$, as the TR increases, the length of the potential core decreases. Similar observation can be found for the setpoints with $M_a \approx 0.9$, i.e., SP07, SP27, and SP46, where SP46 has the shortest potential core and SP07 has the longest.

2. Near-field Flow Statistics

In this subsection, the accuracy of the WMLES in predicting the near-field flow statistics is examined through comparing the computational results with the experimental measurements for each setpoint.

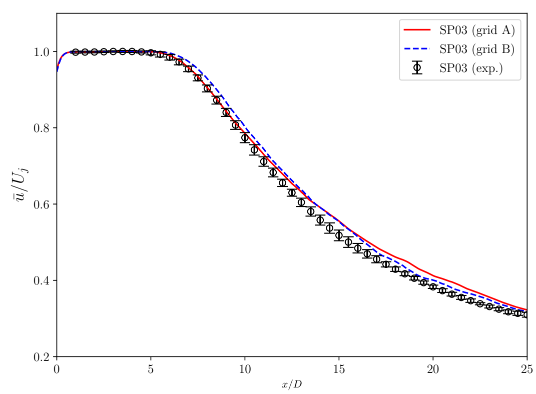

(a) Normalized mean streamwise velocity component along centerline

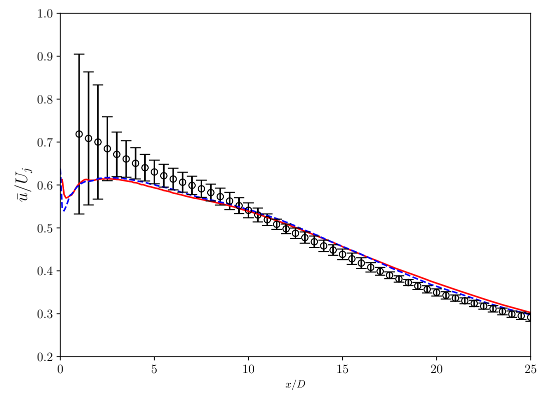

(b) Normalized mean streamwise velocity component along lipline

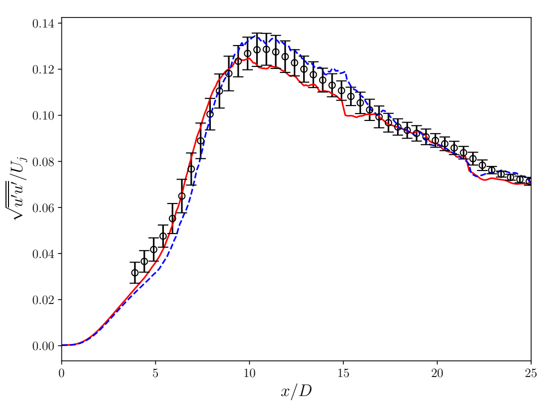

(c) Normalized RMSs along centerline

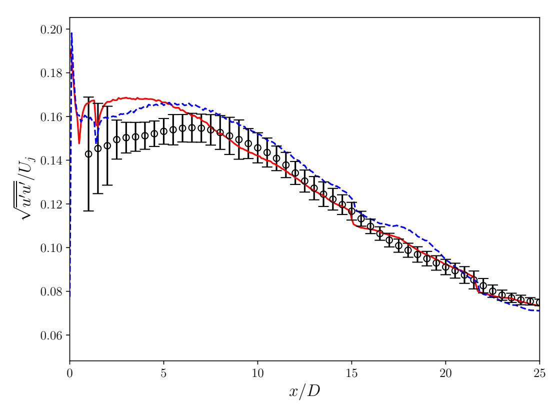

(d) Normalized RMSs along lipline

Fig. 5 Mean streamwise velocity component and root-mean-squares (RMSs) of the fluctuations of the component normalized by the jet velocity magnitude, U_j, along centerline and lipline for the SP03 simulations. Red solid line: grid A; blue dashed line: grid B; black error bars with circles: experiments.

The near-field experimental data is a consensus dataset generated from a process of weighing, averaging, and smoothing of the data from test entries with different test configurations and setups using the Small Hot Jet Acoustic Rig (SHJAR) in NASA Glenn Research Center [21]. The test entries are obtained using two different nozzle geometries, the Acoustic Reference Nozzle with 50.1 mm (2-inch) diameter (ARN2) and the SMC000 nozzle described in the earlier section. Uncertainties of the dataset are estimated from the variations of these test entries for each setpoint. The ARN2 nozzle has a larger contraction compared to the SMC000 nozzle and hence has the tendency of relaminarization of the boundary layer near the exit at low Reynolds number. Reported in [21], the boundary layer of SMC000 is generally more turbulent than that of ARN2 through the measurement of the shape factors for low Mach number (< 0.5) and low Reynolds number jets (< 0.8 million), although the boundary layers of the former is still rarely fully turbulent. It should be noted that the boundary layers are fully turbulent in our simulations because of the tripping near the exit.

Two near-field flow statistics, the mean (time-averaged) streamwise velocity component, $\overline{u}$, and the root-mean-square (RMS) of the fluctuation of the streamwise velocity component, $\sqrt{\overline{u'u'}}$, are chosen for the examination of the WMLES results, where both quantities are normalized with U_j. In Figures 5 and 6, the grid sensitivities of the near-field statistics are studied and compared with the experimental results along the centerline and the lipline for SP03 and SP07 respectively. The lipline results from the computations are averaged azimuthally using 32 angles. For both setpoints, it can be seen that the potential cores of the jet plumes are well-captured as the mean centerline velocity magnitudes achieve the target velocity magnitudes for all simulations and the lengths of the potential cores are well predicted with small grid sensitivities. As the grid resolution is increased, there seems to be a trend to slightly delay the decay of

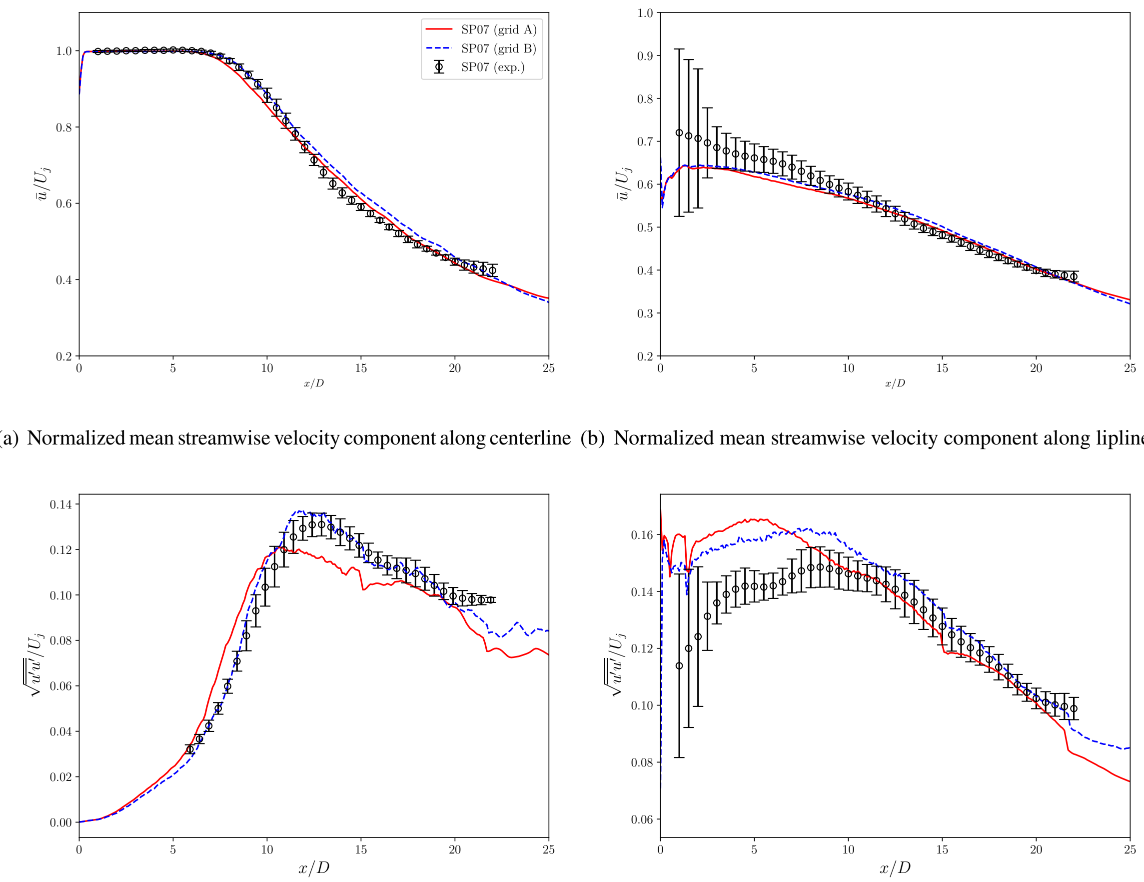

(a) Normalized mean streamwise velocity component along centerline (b) Normalized mean streamwise velocity component along lipline

(c) Normalized RMSs along centerline

(d) Normalized RMSs along lipline

Fig. 6 Mean streamwise velocity component and root-mean-squares (RMSs) of the fluctuations of the component normalized by the jet velocity magnitude, U_j, along centerline and lipline for the SP07 simulations. Red solid line: grid A; blue dashed line: grid B; black error bars with circles: experiments.

the streamwise velocity component at the centerline and the length of the potential core is slightly larger. The lengths of the potential cores are predicted more accurately with grids A and B for SP03 and SP07 respectively. Along both the centerline and lipline, mild over-predictions in the mean streamwise velocity component from the simulations can be seen after the decay of the velocity at $x \approx 11 - 13D$ for both setpoints. In general, the plots show that the grid sensitivities of the mean streamwise velocity component along both centerline and lipline are small for both setpoints and there is a decent agreement between the simulation and experimental results, when the uncertainties of the experiments are also taken into account. The grid sensitivities of the RMSs of the fluctuations of the streamwise velocity component are larger than that of the mean values along both centerline and lipline for both setpoints. The peaks of the RMSs at the centerline obtained using the simulations results with grid A are under-predicted for both SP03 and SP07. Nevertheless, these peaks are better captured when the grid is refined to grid B for both setpoints. This is consistent with the larger RMSs of the streamwise velocity along the lipline when the grid is refined. There are also delays in the growth of the

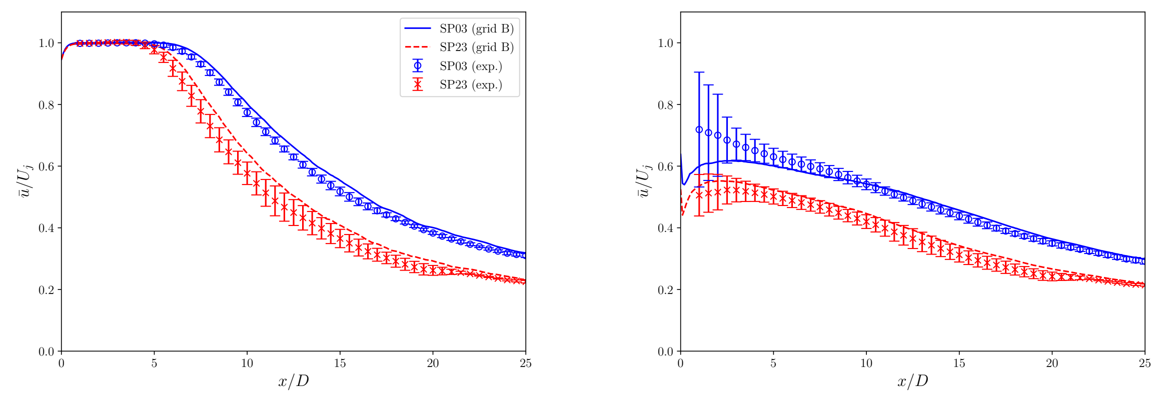

(a) Centerline (b) Lipline

Fig. 7 Mean streamwise velocity component normalized by the jet velocity magnitude, U_j, along centerline and lipline for setpoints with $M_a \approx 0.5$. Blue solid line: SP03 with grid B; red dashed line: SP23 with grid B; blue error bars with circles: SP03 experiment; red error bars with crosses: SP23 experiment.

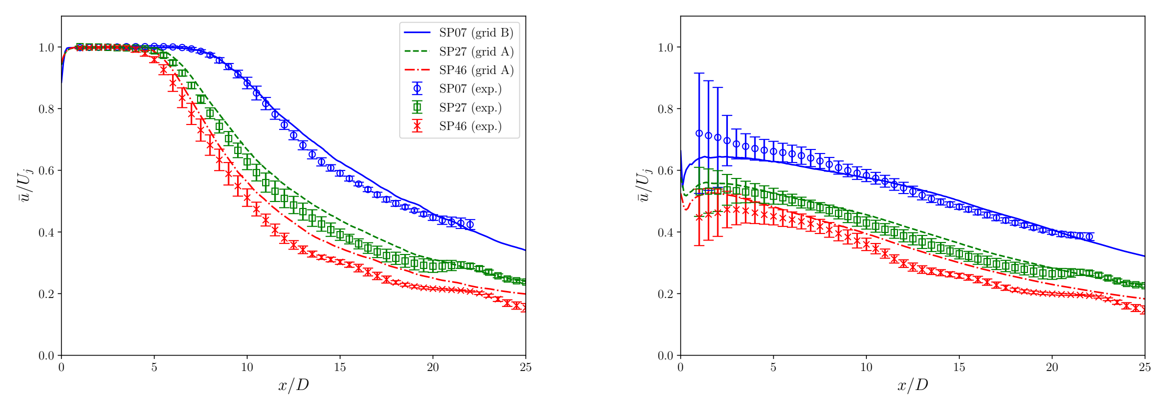

(a) Centerline (b) Lipline

Fig. 8 Mean streamwise velocity component normalized by the jet velocity magnitude, U_j, along centerline and lipline for setpoints with $M_a \approx 0.9$. Blue solid line: SP07 with grid B; green dashed line: SP27 with grid A; red dash-dotted line: SP46 with grid A; blue error bars with circles: SP07 experiment; green error bars with squares: SP27 experiment; red error bars with crosses: SP46 experiment.

velocity fluctuations with grid refinement for both setpoints, and this is similar to the delay in the decay of the mean streamwise velocity magnitude. The simulation results show small sudden falls in the RMSs at around $x = 15D$ and $x = 20.5D$ that are caused by the grid imprinting at the coarse-fine interfaces but the magnitudes of the falls are either similar to or smaller than the error bars of the experimental results. Overall, the RMSs from the computations also agree reasonably well with the experimental results and the effects of the grid resolution on them is not large, barring the statistical variance.

Next, the simulation cases are split into two groups based on the acoustic Mach number, M_a, for further analysis of the capability of the WMLES solver in capturing the thermal effects on the two near-field statistics. The mean streamwise velocity component obtained from the simulations with $M_a \approx 0.5$ and $M_a \approx 0.9$ are shown in Figures 7

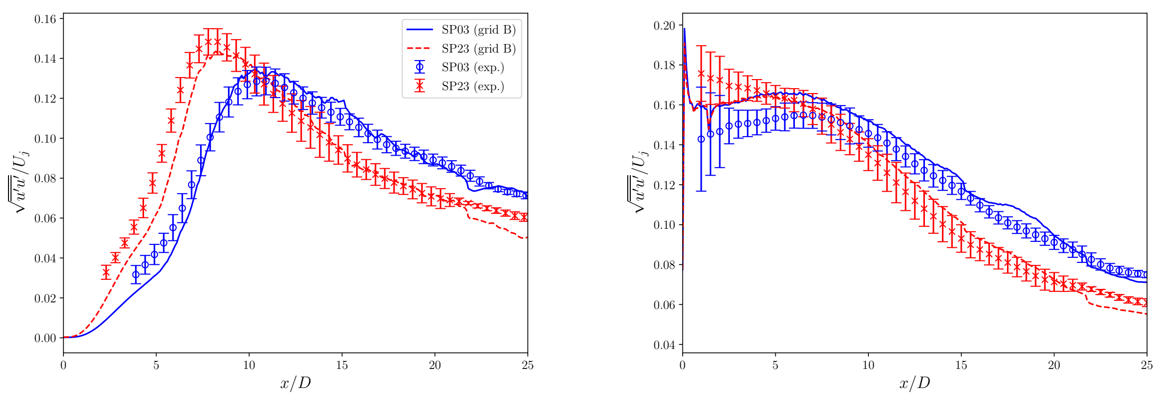

(a) Centerline (b) Lipline

Fig. 9 Root-mean-squares (RMSs) of the fluctuations of the streamwise velocity component normalized by the jet velocity magnitude, U_j, along centerline and lipline for setpoints with $M_a \approx 0.5$. Blue solid line: SP03 with grid B; red dashed line: SP23 with grid B; blue error bars with circles: SP03 experiment; red error bars with crosses: SP23 experiment.

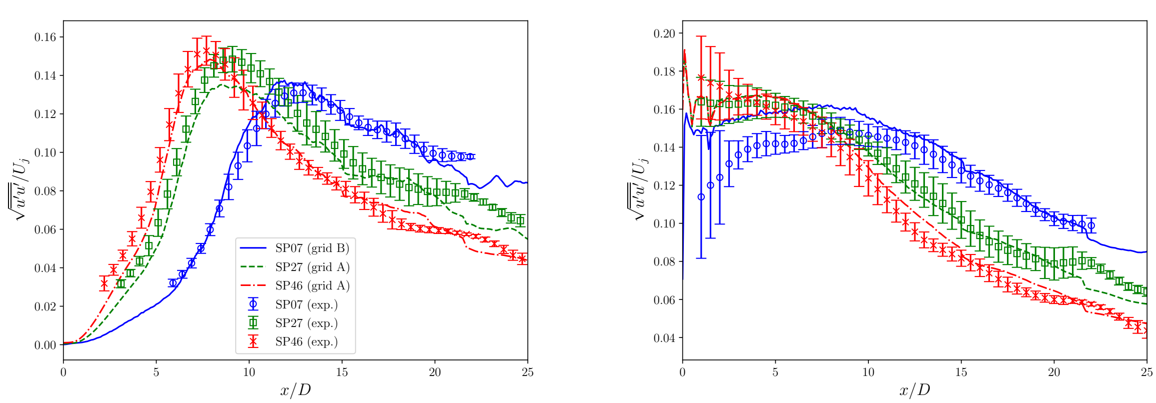

(a) Centerline (b) Lipline

Fig. 10 Root-mean-squares (RMSs) of the fluctuations of the streamwise velocity component normalized by the jet velocity magnitude, U_j, along centerline and lipline for setpoints with $M_a \approx 0.9$. Blue solid line: SP07 with grid B; green dashed line: SP27 with grid A; red dash-dotted line: SP46 with grid A; blue error bars with circles: SP07 experiment; green error bars with squares: SP27 experiment; red error bars with crosses: SP46 experiment.

and 8 respectively. From Figure 7, it is shown that the temperature effects are well captured in the WMLES with $M_a \approx 0.5$. When the TR is raised from SP03 to SP23, the simulation predicts a shorter potential core from the centerline plot with earlier decay of the mean streamwise velocity component. In addition, the downward shift in the normalized mean velocity component along the lipline with the increase in TR is also replicated accurately in these simulations. As for the simulations with $M_a \approx 0.9$, it can be seen from Figure 8 that the thermal effects from the increase in TR are also well captured in the simulations of SP07, SP27, and SP46. These effects include the reduction in the potential core length shown in the centerline plot and the downshift of the normalized mean streamwise velocity component along the lipline with the raise in TR. However, there is larger over-prediction in the streamwise velocity component along both centerline and lipline when the TR is higher. In Figures 9 and 10, the capability of the WMLES in predicting the effect of TR on the RMSs of the fluctuation of the streamwise velocity component is studied. As shown in Figure 9, the effects of TR on the RMSs along both centerline and lipline for SP03 and SP23 are accurately simulated in these simulations. Specifically, the peaks and the peak locations along the centerline are captured well. Similarly, the RMSs along the centerline are reproduced accurately in the set of simulations with $M_a \approx 0.9$ in Figure 10. Although there is some degree of over-prediction in the RMS from the lip location to $x \approx 12D$ along the lipline for the cold jet case SP07, the simulation results of the hot jet cases SP27 and SP46 agree well with the experiment. To sum up, the thermal effects introduced by the TR on the near-field flows are well represented in these WMLES for two groups of setpoints with very different M_a.

B. Far-field Acoustics Predictions

The time-domain Ffowcs Williams–Hawkings (FWH) acoustic analogy [29] in the permeable/porous form [30, 31] is applied to approximate the far-field noise with the near-field CFD data. The details of the permeable FWH acoustic analogy is given in Appendix A. The time-domain FWH method is implemented in Volcano ScaLES as a streaming algorithm where acoustics can be propagated on-the-fly to far-field microphone locations using the near-field data sampled on single/multiple set(s) of FWH surfaces during the simulations, without the need to output the surface data to the hard disk for a later post-processing. This completely removes the need of large disk space for storing the FWH surface data and also reduces the input/output (IO) cost to write/read the surface data to/from the disk that may become

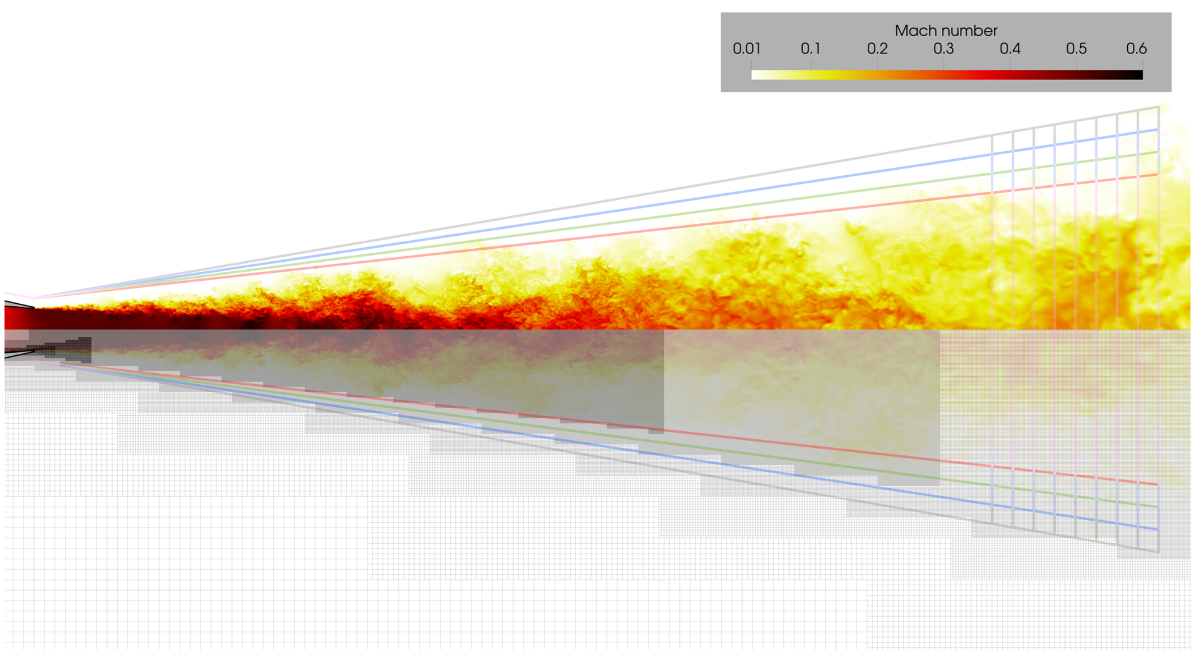

Fig. 11 Location of the four FWH surfaces with endcaps at the center-plane which also shows the instantaneous Mach number contours for SP03 with grid B. Red lines: very tight FWH surface; green lines: tight FWH surface; blue lines: wide FWH surface; gray lines: very wide FWH surface. The overlapped region of the FWH surfaces is shown in pink. The grid is shown in the bottom half of the figure.

bottlenecks of the simulations and post-processing.

Four sets of FWH surfaces, depicted in Figure 11, are used for the study of the sensitivity of the far-field noise predictions on the FWH location with the porous FWH method. The upstream geometries of the four porous FWH surface sets are the same which is a $0.25D$ (12.7 mm) offset of the outer nozzle geometry, but they have different slopes for the downstream tapered cylindrical surfaces. The four sets of FWH surfaces are labelled as very tight, tight, wide, and very wide surfaces which have slopes of 0.11, 0.13, 0.15, and 0.17 respectively. Each set of porous FWH surfaces consists of 9 staggered endcaps (disks), which are separated from each other by a distance of $0.5D$, in the range from $x = 23D$ to $27D$. The far-field pressure fluctuations are averaged on these endcaps, as a filtering process to reduce the spurious low-frequency noise generated when the turbulent jet passes through the endcaps of the FWH surface [32, 33]. Note that these endcaps are all located in a uniform grid region. In all of these simulations, the sampling interval is 3.33% CTU. The one-third octave power spectra are computed using the Welch's method where the time signals are truncated into bins (segments) with a bin interval of 100 CTUs and 75% overlap and the spectra are averaged over the bins. To avoid spectral leakage, the Hann windowing is used for filtering time signal in each bin.

In the experiments, there are 24 microphones to collect the far-field noise from angles of 50° (upstream) to 165° (downstream). These far-field noise data are generated using the SMC000 nozzle and are also normalized to be at a

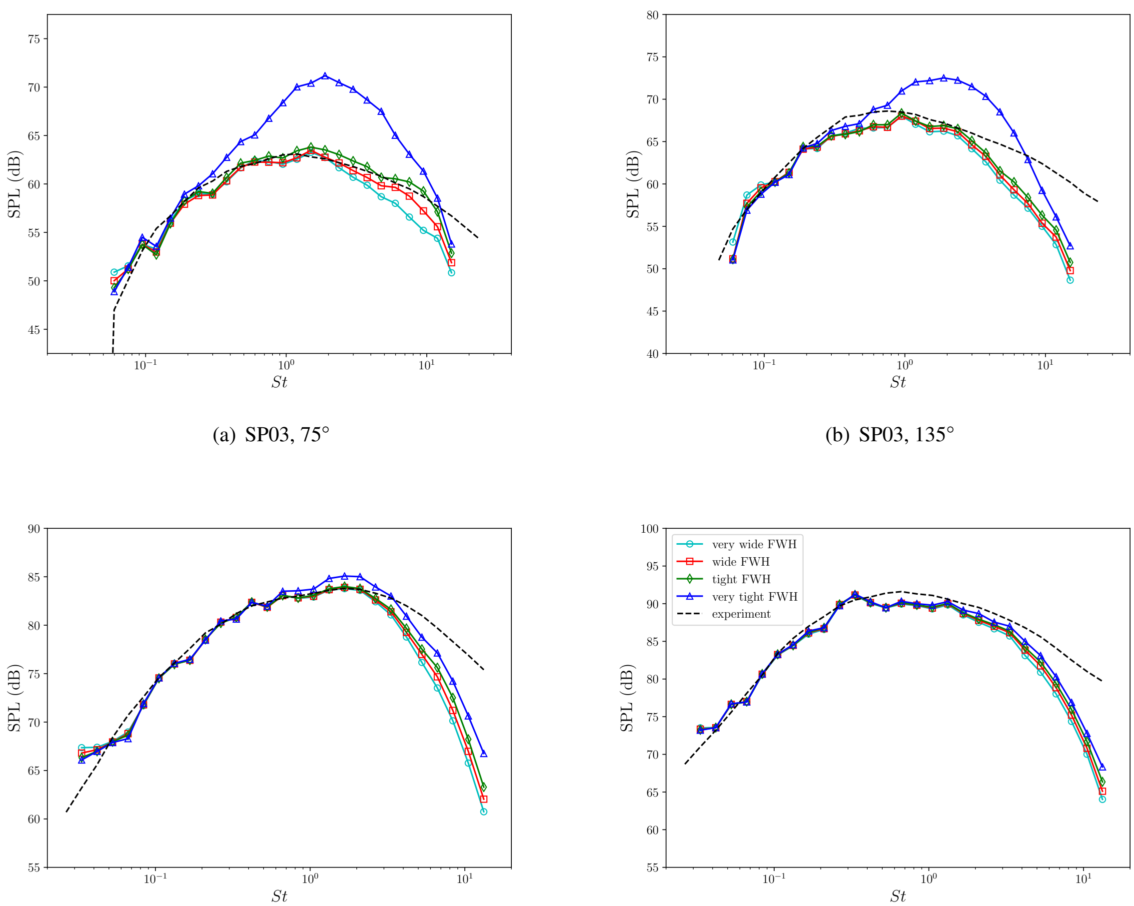

(a) SP03, 75°

(b) SP03, 135°

(c) SP07, 75°

(d) SP07, 135°

Fig. 12 Sensitivity of the far-field sound pressure level (SPL) at different angles to the FWH surface location for the cases SP03 and SP07 with grid B. Cyan solid line with circles: very wide FWH surface set; red solid line with squares: wide FWH surface set; green solid line with diamonds: tight FWH surface set; blue solid line with triangles: very tight FWH surface set; black dashed line: experiments.

distance of $100D$ away from the nozzle exit for validation of CFD/CAA codes [20]. Figure 12 shows the sensitivity of the far-field noise at some of these microphone locations on the positions of the FWH surfaces for two chosen setpoints, SP03 and SP07, computed with grid B. For SP03, when the very tight FWH surface set is used, large over-predictions are observed for Strouhal number, $St = f \cdot \text{CTU}$, starting from 0.3 at different angles, compared with the experimental results, where f is the frequency. The noise level in the medium frequency range for the higher M_a setpoint, SP07, is also over that of the experimental measurements but the over-prediction is smaller. It is believed that when the very tight FWH surface set is used, the surface crosses the jet too aggressively and spurious noise is generated when the turbulent eddies pass through the downstream radial surface. When the downstream conically FWH surface is wider (radially larger), the contamination of the spectra is largely reduced. The over-prediction is improved by a lot for spectra computed using the radially larger FWH surfaces, i.e., the tight, wide, and very wide surface sets, and their results are quite close to each other except that the noise level in the high frequency range decreases when a wider (radially larger) FWH surface set is used. In the remaining part of this work, the wide and tight FWH surface sets are used respectively for setpoints with $M_a \approx 0.5$ (SP03 and SP23) and $M_a \approx 0.9$ (SP07, SP27, and SP46) respectively.

Figure 13 examines the capability of the porous FWH approach coupled with the WMLES results in predicting the effects of M_a on the far-field noise at different angles for the two isothermal setpoints with TR $\approx$ 1, SP03 and SP07.

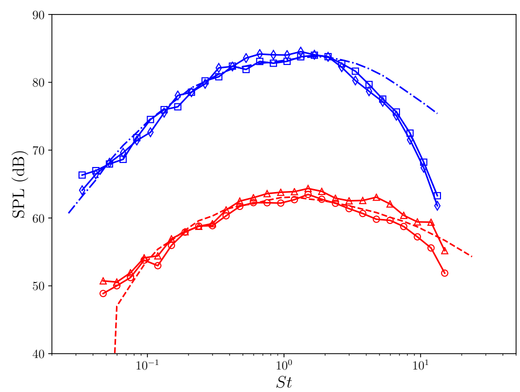

(a) 75°

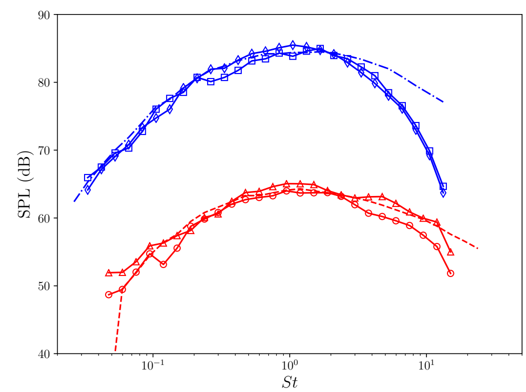

(b) 90°

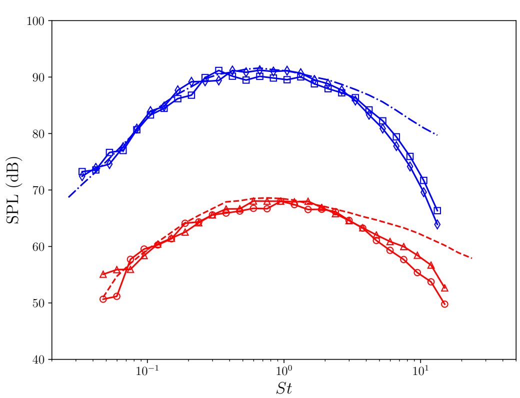

(c) 135°

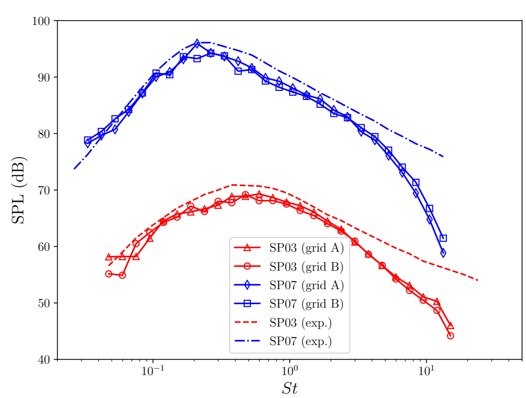

(d) 150°

Fig. 13 Effect of the acoustic Mach number, M_a, on the far-field sound pressure level (SPL) at different angles for the setpoints with isothermal jets at TR ≈ 1. Red line with triangles: SP03 with grid A; red line with circles: SP03 with grid B; blue line with diamonds: SP07 with grid A; blue line with squares: SP07 with grid B; red dashed line: SP03 experiment; blue dash-dotted line: SP07 experiment.

From the plots, the experimental results show that when M_a is increased from 0.5 to 0.9 (from SP03 to SP07), there is a large increase in the sound level over the entire frequency range of interest for each angle. In general, the effects of M_a on the far-field noise predictions are well captured by these WMLES at different angles in the low and medium ranges of frequency and the low-frequency noise has small grid sensitivity. The spectra computed using grid A are better statistically converged in the low frequency range because of longer sampling time (over 1200 CTUs) compared to that with grid B (over 600 CTUs). The noise level in the medium frequency range is slightly over-predicted at 75° for SP03 with grid A but is improved when the finer grid B is used. However, as the grid A is refined to grid B, the high-frequency noise level becomes under-predicted at 90°. At the higher angles, 90° and 150°, the spectra have smaller grid sensitivities. The spectra falls off quickly in the high frequency range ($St > 2$) for SP07 at all angles no matter whether grids A or B are used, although the noise level is slightly higher in that range when the grid A is refined to grid B. In general, the far-field SPL spectra are well-captured using these WMLES with the permeable FWH acoustic analogy from $St \approx 0.1$ to $St \approx 2$ for these two setpoints. Similar comparison is presented in Figure 14 for two setpoints with hotter jets, SP23 and SP27, where TR ≈ 1.8. These plots at different angles also indicate that the setpoint with higher M_a, i.e., SP27, produces higher noise levels in the experiments compared to SP23 and this effect is generally captured in the simulations in the low and medium frequency ranges up to $St \approx 2$. A general improvement on the over-estimation of spectrum in the range $1 < St < 10$ is also shown for SP23 at 75° when grid A is refined to grid B,

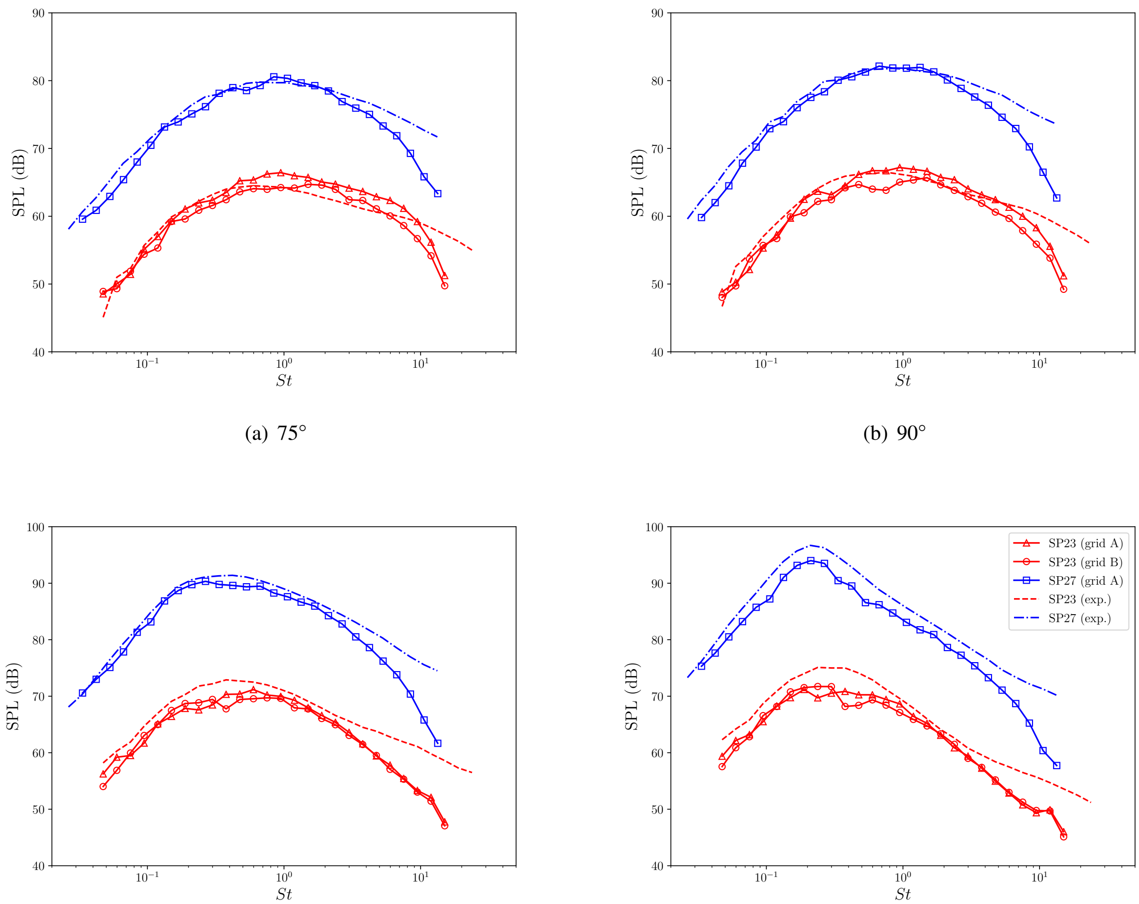

(a) 75° (b) 90°

(c) 135° (d) 150°

Fig. 14 Effect of the acoustic Mach number, M_a, on the far-field sound pressure level (SPL) at different angles for the setpoints with hot jets at TR $\approx$ 1.8. Red line with circles: SP23 with grid A; blue line with squares: SP27 with grid A; red dashed line: SP23 experiment; blue dash-dotted line: SP27 experiment.

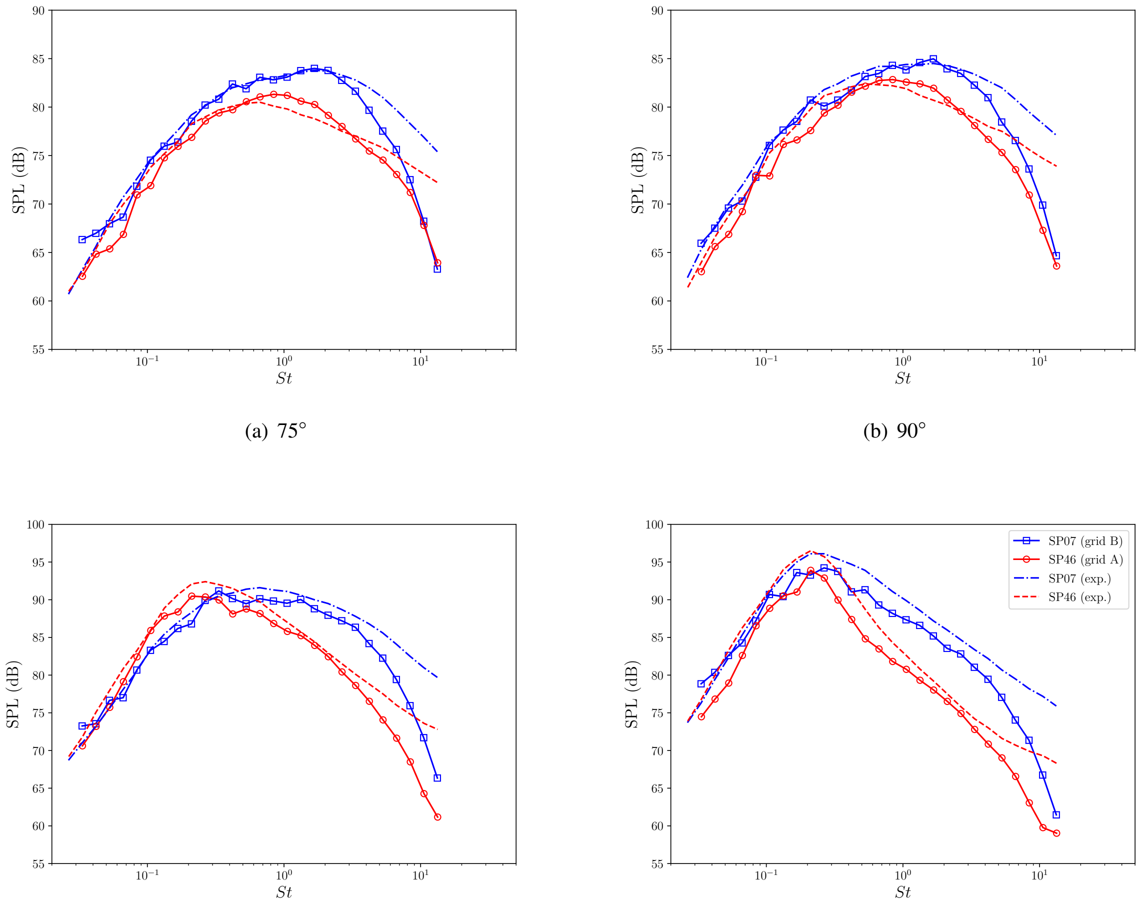

(a) 75°

(b) 90°

(c) 135°

(d) 150°

Fig. 15 Effect of the ratio of jet temperature to ambient temperature, TR, on the far-field sound pressure level (SPL) at different angles for the setpoints with $M_a \approx 0.9$. Blue line with squares: SP07 with grid B; red line with circles: SP46 with grid A; blue dash-dotted line: SP07 experiment; red dashed line: SP46 experiment.

although the spectra is slightly under-predicted in the same frequency range at 90°.

Figure 15 shows the thermal effect on the far-field acoustics by comparing the far-field spectra of SP07 and SP46, where both have $M_a \approx 0.9$ but the former has TR ≈ 1 while the latter has TR ≈ 2.7. While the spectra in the high frequency range, $St > 2$, is largely under-predicted by the simulations, probably due to lack of grid resolution, the low- and medium-frequency noise levels are reasonably predicted in the simulations. The experimental results suggest that the low-frequency noise levels below $St < 0.1$ are similar between the isothermal (SP07) and heated (SP46) jets but the isothermal jet case produces louder sound waves in the higher frequency range at all angles. These thermal effects on the far-field noise is well captured with the permeable FWH method applied on the WMLES results in the low and medium frequency ranges.

V. Concluding Remarks

WMLES of subsonic jets exhausted from an axisymmetric nozzle were conducted using an octree Cartesian solver with the immersed boundary approach. These cases are selected from the NASA's experimental dataset using the SMC000 nozzle. In total, five setpoints with acoustic Mach number ranging from 0.5 to 0.9 are considered where two of them are essentially isothermal while another three setpoints have heated jets with temperature ratios up to 2.7.

Thanks to the largely optimized memory management of the solver and the use of numerical methods with low memory footprint implemented in Volcano ScaLES, WMLES with over 500 million cells could be conducted on a workstation with only two GPU cards. In general, the grid sensitivities in the near-field statistics were found to be small, barring the variations in the experimental results. Reasonably good agreement between the simulation and experimental results can be seen for the near-field flow fields, such as the mean velocity and the RMS of the velocity fluctuations, with some discrepancies that may be caused by the uncertainty in the boundary layer state in the experiments. Under the same acoustic Mach number, the thermal effect on the near-field statistics are well reproduced in the WMLES. The permeable or porous time-domain FWH acoustic analogy was used to radiate the near-field CFD data to far-field microphone locations on-the-fly during the simulations. It was observed that while the noise spectra in the low frequency range are well captured using the WMLES coupled with the FWH approach, the predictions of the medium and high-frequency noise is quite sensitive to the location of the FWH surfaces and the grid resolution. Special care has to be taken such that the turbulent eddies do not pass through the radially surface to contaminate the noise predictions, even when proper endcap-averaging process is used to eliminate the spurious sound generated when turbulent eddies leave the FWH endcaps. When the FWH surfaces are suitably placed to enclose the turbulent jet plumes, reasonably good comparison between the far-field noise predictions and the experimental measurements was seen, up to a Strouhal number of around 2. The Mach number and the thermal effects on the far-field low- and medium-frequency noise levels at different angles are also well captured in these scale-resolving simulations.

It is expected that the new scale-resolving Cartesian methodology can also be used for studying the flows and acoustics of jets exhausted from more complex nozzle geometries, such as multi-stream nozzles, nozzles with chevrons, etc., and the installation effects on the aerodynamics and aeroacoustics from the interaction between the jet plumes and the aerodynamic devices.

Acknowledgments

We would like to thank Dr. James Bridges and Dr. Nicholas Georgiadis from NASA Glenn Research Center for the help on providing the geometry of the NASA's SMC000 nozzle.

A. Time-domain Permeable Ffowcs Williams–Hawkings (FWH) Acoustic Analogy

Consider a moving body immersed in a fluid with quiescent ambient state, the FWH equation for a permeable surface described by $f(\boldsymbol{x}, t) = 0$ is given by [30]

$$\Box^2 \left(c_0^2 \rho'\right) = \frac{\partial}{\partial t} \left[Q_n \delta\left(f\right)\right] - \frac{\partial}{\partial x_i} \left[L_i \delta f\right] + \frac{\partial^2}{\partial x_i \partial x_j} \left[T_{ij} H\left(f\right)\right], \tag{1}$$

where $Q_n = Q_i \hat{n}_i$ and $L_i = L_{ij} \hat{n}_j$. Q_i and L_{ij} are defined as

$$Q_i = \rho_0 v_i + \rho\left(u_i - v_i\right), \tag{2}$$

$$L_{ij} = P'_{ij} + \rho u_i \left(u_j - v_j\right). \tag{3}$$

$\Box^2 = c_0^{-2} \partial^2 / \partial t^2 - \nabla^2$ is the wave operator with the ambient sound speed c_0. f is normalized in a way such that $|\nabla f| = 1$. As a result, $\boldsymbol{n} = \nabla f$ is the outward unit vector normal to the FWH surface. $H(f)$ is the Heaviside function and $\delta f = H'(f)$ is the Dirac delta function. $\rho' = \rho - \rho_0$ is the fluctuation of the density ρ from the ambient density $\rho_0 = \rho_\infty$. u_i and v_i are the velocities of the fluid and the surface respectively. $P'_{ij} = P_{ij} - p_0 \delta_{ij}$ is the perturbation compressible stress tensor where $p_0 = p_\infty$ is the ambient pressure in this work and δ_{ij} is the Kronecker delta. The compressible stress tensor P_{ij} and the Lighthill stress tensor T_{ij} are given by

$$P_{ij} = p \delta_{ij} - \tau_{ij}, \tag{4}$$

$$T_{ij} = \rho u_i u_j + P'_{ij} - c_0^2 \rho' \delta_{ij}, \tag{5}$$

where p and τ_{ij} are the pressure and viscous stress tensor respectively. Note that Equation (1) is an exact rearrangement of the density and momentum equations of the Navier–Stokes equations.

The integral solution of Equation (1) for the acoustic pressure or pressure fluctuation, $p' = p - p_0$, at the observer position $\boldsymbol{x}$ and observer time t can be derived using the free-space Green's function:

$$c_0^2 \rho'\left(\boldsymbol{x}, t\right) = p'\left(\boldsymbol{x}, t\right) = p'_T\left(\boldsymbol{x}, t\right) + p'_L\left(\boldsymbol{x}, t\right) + p'_Q\left(\boldsymbol{x}, t\right), \tag{6}$$

where $p'_T(\boldsymbol{x},t)$, $p'_L(\boldsymbol{x},t)$, and $p'_Q(\boldsymbol{x},t)$ are the thickness, loading, and quadrupole terms respectively. The left equality $p' = c_0^2\rho'$ comes from the assumption that the observer is sufficiently far away from the acoustic source region and the fluctuations are small. The quadrupole component p'_Q requires volume integration of the quadrupole term (last term in the right hand side of Equation (1)) outside the FWH surface and is neglected. The viscous stress tensor τ_{ij} in P_{ij} is also neglected as it is generally a negligible source of noise.

In this study, the permeable FWH approach is used with the restriction that the permeable surface is in uniform rectilinear motion. The permeable FWH approach [30, 31] is implemented in a similar form as the formulation 1A of the solid FWH approch [34] as a streaming algorithm:

$$4\pi p'_T(\boldsymbol{x},t) = 4\pi c_0^2\rho'_T(\boldsymbol{x},t) = \int_{f=0}\left[\frac{\dot{Q}_n}{R\left(1-M_R\right)^2}\right]_{ret} dS + \int_{f=0}\left[\frac{Q_n c_0\left(M_R - M^2\right)}{R^2\left(1-M_R\right)^3}\right]_{ret} dS, \tag{7}$$

$$4\pi p'_L(\boldsymbol{x},t) = 4\pi c_0^2\rho'_L = \frac{1}{c_0}\int_{f=0}\left[\frac{\dot{L}_R}{R\left(1-M_R\right)^2}\right]_{ret} dS + \int_{f=0}\left[\frac{L_R - L_M}{R^2\left(1-M_R\right)^2}\right]_{ret} dS + \int_{f=0}\left[\frac{L_R\left(M_R - M^2\right)}{R^2\left(1-M_R\right)^3}\right]_{ret} dS. \tag{8}$$

The subscript "ret" denotes integration at the retarded or emission time τ of the surface elements. $M_i = v_i/c_0$ is the Mach number vector of the moving surface. Other terms in the solutions are defined as

$$M^2 = M_i M_i, \quad M_R = M_i \hat{R}_i, \tag{9}$$

$$L_R = L_i \hat{R}_i, \quad L_M = L_i M_i, \quad \dot{L}_R = \frac{\partial L_i}{\partial \tau}\hat{R}_i, \tag{10}$$

where $R = |\boldsymbol{x} - \boldsymbol{y}|$ is the acoustic distance between the observer and the source (any surface element) at the retarded time and $\boldsymbol{R} = \nabla R/|\nabla R|$ is the unit radiation vector. The formulation above assumes that both the observer and the source move at the same velocity such that R and $\boldsymbol{R}$ are constant in time.

In a wind tunnel configuration, the problem can be further simplified by assuming the flow is in the x_1 direction with speed U_0 and Mach number M_0. For subsonic flow, the Garrick triangle [35, 36] can be used to compute the retarded time and the acoustic distance between the observer and the source.

References

[1] Huff, D. L., "Noise reduction technologies for turbofan engines," *35th International Congress and Exposition on Noise Control Engineering (INTER-NOISE 2006)*, 2007.

[2] Thomas, R. H., Guo, Y., Berton, J., and Fernandez, H., "Aircraft noise reduction technology roadmap toward achieving the nasa 2035 goal," *23rd AIAA/CEAS aeroacoustics conference*, 2017, p. 3193.

[3] Krein, A., and Williams, G., "Flightpath 2050: Europe's vision for aeronautics," *Innovation for Sustainable Aviation in a Global Environment: Proceedings of the Sixth European Aeronautics Days, Madrid*, Vol. 30, 2012.

[4] Lighthill, M. J., "On sound generated aerodynamically II. Turbulence as a source of sound," *Proceedings of the Royal Society of London. Series A. Mathematical and Physical Sciences*, Vol. 222, No. 1148, 1954, pp. 1–32.

[5] Brown, C. A., "Jet-surface interaction test: far-field noise results," *Journal of Engineering for Gas Turbines and Power*, Vol. 135, No. 7, 2013, p. 071201.

[6] Rego, L., Avallone, F., Ragni, D., and Casalino, D., "Jet-installation noise and near-field characteristics of jet–surface interaction," *Journal of Fluid Mechanics*, Vol. 895, 2020, p. A2.

[7] Bodony, D. J., and Lele, S. K., "Current status of jet noise predictions using large-eddy simulation," *AIAA journal*, Vol. 46, No. 2, 2008, pp. 364–380.

[8] Brès, G. A., and Lele, S. K., "Modelling of jet noise: a perspective from large-eddy simulations," *Philosophical Transactions of the Royal Society A*, Vol. 377, No. 2159, 2019, p. 20190081.

[9] Housman, J. A., Stich, G.-D., and Kiris, C. C., "Jet noise prediction using hybrid RANS/LES with structured overset grids," *23rd AIAA/CEAS Aeroacoustics Conference*, 2017, p. 3213.

[10] Stich, G.-D., Ghate, A. S., Housman, J. A., and Kiris, C. C., "Wall Modeled Large Eddy Simulations for NASA's jet noise consensus database of single-stream, round, convergent jets." *AIAA SCITECH 2022 Forum*, 2022, p. 0684.

[11] Bres, G. A., Bose, S. T., Emory, M., Ham, F. E., Schmidt, O. T., Rigas, G., and Colonius, T., "Large-eddy simulations of co-annular turbulent jet using a Voronoi-based mesh generation framework," *2018 AIAA/CEAS Aeroacoustics Conference*, 2018, p. 3302.

[12] Casalino, D., and Lele, S., "Lattice-Boltzmann simulation of coaxial jet noise generation," *Proceedings of the Summer Program*, Center for Turbulence Research Stanford, CA, 2014, pp. 231–240.

[13] van der Velden, W., Casalino, D., Gopalakrishnan, P., Jammalamadaka, A., Li, Y., Zhang, R., and Chen, H., "Validation of jet noise simulations and resulting insights of acoustic near field," *AIAA Journal*, Vol. 57, No. 12, 2019, pp. 5156–5167.

[14] Aikens, K. M., Dhamankar, N. S., Martha, C. S., Situ, Y., Blaisdell, G. A., Lyrintzis, A. S., and Li, Z., "Equilibrium wall model for large eddy simulations of jets for aeroacoustics," *52nd Aerospace Sciences Meeting*, 2014, p. 0180.

[15] Le Bras, S., Deniau, H., Bogey, C., and Daviller, G., "Development of compressible large-eddy simulations combining high-order schemes and wall modeling," *AIAA Journal*, Vol. 55, No. 4, 2017, pp. 1152–1163.

[16] Schmidt, O. T., Towne, A., Colonius, T., Cavalieri, A. V., Jordan, P., and Bres, G. A., "Wavepackets and trapped acoustic modes in a turbulent jet: coherent structure eduction and global stability," *Journal of Fluid Mechanics*, Vol. 825, 2017, pp. 1153–1181.

[17] Brès, G. A., Jordan, P., Jaunet, V., Le Rallic, M., Cavalieri, A. V., Towne, A., Lele, S. K., Colonius, T., and Schmidt, O. T., "Importance of the nozzle-exit boundary-layer state in subsonic turbulent jets," *Journal of Fluid Mechanics*, Vol. 851, 2018, pp. 83–124.

[18] Wu, G. J., Lele, S. K., Jeun, J., Gustavsson, J., Sellappan, P., and Kumar, R., "Unstructured large-eddy simulations of rectangular jet screech: assessment and validation," *AIAA Journal*, Vol. 61, No. 3, 2023, pp. 1224–1237.

[19] Wernet, M. P., and Bridges, J. E., "Characterization of Chevron Nozzle Performance," Tech. rep., 2021.

[20] Brown, C., and Bridges, J., "Small hot jet acoustic rig validation," Tech. Rep. TM-2006-214234, NASA, 2006.

[21] Bridges, J., and Wernet, M., "Establishing consensus turbulence statistics for hot subsonic jets," *16th AIAA/CEAS aeroacoustics conference*, 2010, p. 3751.

[22] Shu, C.-W., and Osher, S., "Efficient implementation of essentially non-oscillatory shock-capturing schemes, II," *Journal of Computational Physics*, Vol. 83, No. 1, 1989, pp. 32–78.

[23] Vreman, A., "An eddy-viscosity subgrid-scale model for turbulent shear flow: Algebraic theory and applications," *Physics of fluids*, Vol. 16, No. 10, 2004, pp. 3670–3681.

[24] Wong, M. L., Ghate, A. S., Kenway, G. K. W., Angel, J. B., and Kiris, C. C., "Immersed Boundary Wall-Modelled Large Eddy Simulations of a Nose Landing Gear for Aeroacoustics," *AIAA Aviation 2024 Forum*, 2024.

[25] Kenway, G. K. W., Ghate, A. S., Browne, O. M. F., Wong, M. L., Angel, J. B., and Kiris, C. C., "Immersed Boundary Wall-Modelled Large Eddy Simulations of a Generic Hammerhead Payload Fairing," *AIAA Aviation 2024 Forum*, 2024.

[26] Wong, M. L., Ghate, A. S., Kenway, G. K. W., Angel, J. B., and Kiris, C. C., "Immersed Boundary Wall-Modelled Large Eddy Simulations of Straight Wings with Three-Dimensional Ice Accretion," *AIAA Aviation 2024 Forum*, 2024.

[27] Angel, J. B., Ghate, A. S., Kenway, G. K. W., Wong, M. L., Browne, O. M. F., and Kiris, C. C., "Validation of Immersed Boundary Wall-Modelled Large Eddy Simulations with F-16XL Flight Data," *AIAA Aviation 2024 Forum*, 2024.

[28] Angel, J. B., Ghate, A. S., Kenway, G. K. W., Wong, M. L., and Kiris, C. C., "Immersed Boundary Wall-Modelled Large Eddy Simulations for Automotive Aerodynamics," *AIAA Aviation 2024 Forum*, 2024.

[29] Williams, J. F., and Hawkings, D. L., "Sound generation by turbulence and surfaces in arbitrary motion," *Philosophical Transactions for the Royal Society of London. Series A, Mathematical and Physical Sciences*, 1969, pp. 321–342.

[30] Di Francescantonio, P., "A new boundary integral formulation for the prediction of sound radiation," *Journal of Sound and Vibration*, Vol. 202, No. 4, 1997, pp. 491–509.

[31] Brentner, K. S., and Farassat, F., "Analytical comparison of the acoustic analogy and Kirchhoff formulation for moving surfaces," *AIAA journal*, Vol. 36, No. 8, 1998, pp. 1379–1386.

[32] Shur, M. L., Spalart, P. R., and Strelets, M. K., "Noise prediction for increasingly complex jets. Part I: Methods and tests," *International journal of aeroacoustics*, Vol. 4, No. 3, 2005, pp. 213–245.

[33] Mendez, S., Shoeybi, M., Lele, S., and Moin, P., "On the use of the Ffowcs Williams-Hawkings equation to predict far-field jet noise from large-eddy simulations," *International Journal of Aeroacoustics*, Vol. 12, No. 1-2, 2013, pp. 1–20.

[34] Farassat, F., and Succi, G. P., "The prediction of helicopter rotor discrete frequency noise," *In: American Helicopter Society*, 1982, pp. 497–507.

[35] Garrick, I., and Watkins, C. E., "A theoretical study of the effect of forward speed on the free-space sound-pressure field around propellers," Tech. rep., 1953.

[36] Lockard, D., "A comparison of Ffowcs Williams-Hawkings solvers for airframe noise applications," *8th AIAA/CEAS Aeroacoustics Conference & Exhibit*, 2002, p. 2580.